Article

Effects of Different CO_2 Concentrations and Degradation Media on Static Corrosion of Commercially Pure Zinc

Souhila Ould-Mohamed [1], **Sofia Gambaro** [2], **Ana Laura Ramirez-Ledesma** [3], **Carlo Paternoster** [1] **and Diego Mantovani** [1,*]

1   Lab Biomaterials and Bioengineering, CRC Tier I. Department of Mining, Metallurgy and Materials Engineering & CHU de Québec Research Center, Division of Regenerative Medicine, Laval University, Quebec City, QC G1V 0A6, Canada; souhila.ould-mohamed.1@ulaval.ca (S.O.-M.); carlo.paternoster.1@ulaval.ca (C.P.)

2   National Research Council, Institute of Condensed Matter Chemistry and Technologies for Energy, CNR-ICMATE, 16149 Genoa, Italy; sofia.gambaro@ge.icmate.cnr.it

3   Departamento de Ingeniería Metalúrgica, Facultad de Química, Universidad Nacional Autónoma de México, Ciudad de México 04510, Mexico; alramirez1303@comunidad.unam.mx

*   Correspondence: diego.mantovani@gmn.ulaval.ca

Abstract: Zn alloys have lately captivated the attention of the scientific community as possible materials for cardiovascular applications, showing a corrosion behavior and mechanical properties in between of those of Mg and Fe alloys. To better understand the different aspects of the interaction of Zn with body fluids, the basic corrosion pattern and the degradation products' formation were investigated considering the effect of CO_2 amount in the atmosphere and different pseudo-physiological media; that is Hanks' balanced salt (HSS), Dulbecco's phosphate-buffered saline (PSS) and physiological saline solution (NSS), through a 14-day static immersion study. A mixed degradation layer mainly composed of ZnO with $Zn_3(PO_4)_2 \cdot 4H_2O$ and $Zn(CO_3)_2$ precipitates was found on surfaces immersed in both HSS and PSS, independently of the atmosphere, while a $ZnO/ZnCl_2$ layer was found on the surface immersed in NSS, which also revealed the higher corrosion rate due to the effect of Cl^- ions. Samples tested under a CO_2-rich atmosphere showed a more compact passivating layer, higher dimensions crystals and less cavities when tested in HSS, PSS and NSS, respectively.

Keywords: Zn-based alloys; biodegradable; in vitro degradation; CO_2-atmosphere; corrosion rate

1. Introduction

Degradable metallic devices for biomedical applications need to support tissue regeneration through a set of appropriate mechanical properties. This function can be accomplished by re-absorbable metallic materials, which present the advantage of a tuned dissolution in the human body. In fact, a re-absorbable alloy is expected to allow not only tissue healing during the required period, but also withstand a process of gradual degradation, and finally a full disappearing when the recovering process is completed [1]. In addition, as these alloys are subjected to corrosion inside the human body, their degradation products need to be non-toxic, both locally and systemically [2]. Currently, three groups of re-absorbable alloys are under intensive research for these applications: Fe-, Mg- and Zn-based, respectively [2,3]. Firstly, pure Fe was deeply investigated for its interesting mechanical properties [4], the absence of systemic and local toxicity [5], and the absence of long-term adverse effects after implantation [6] while the low corrosion rate was universally recognized as the main disadvantage [7]. The introduction of Mn allowed the increase of the degradation rate of Fe-based alloys, so that the corrosion rate would span in the range 515–520 μm/year, about twice faster than that of pure Fe [8,9]; this was found for an Fe-12Mn-1.2C alloy, leading to a general improvement of the mechanical properties and to a lower corrosion rate, approximatively of 0.20 ± 0.05 mm/year [10]. The formation of a

degradation product layer on sample surfaces, after static degradation tests, especially for higher amounts of Mn, was assessed considering different environmental conditions, such as 5 vol.% CO_2 [11–13]. However, even the corrosion rate of this group of alloys, with or without C, is generally considered too low for many temporary implant applications [3]. Furthermore, the formation of stable degradation products, such as Fe oxides, phosphates and carbonates, and Mn phosphates, carbonates and hydroxides [14], in a physiological environment, could be dangerous due to their local and systemic accumulation [15]. Mg-based alloys were intensely studied during the last decades [16] as Mg is an essential trace element [17] and its ions are used in many cellular functions [18]. Even if pure Mg (Mg = 99.9 wt.%; Fe < 40 ppm) shows a good thrombogenicity and appropriate biocompatibility toward a wide number of cell lines [19], however, its mechanical properties are in general lower than those of Fe-based alloys, for what concerns the elastic modulus [20], yielding strength [21], ultimate tensile strength and elongation at rupture [22]. Alloying elements are then commonly adopted to reach materials with the desired mechanical features; among them, in particular, rare earths are added to Mg due to the formation of highly stable strengthening phases as well as the activation of additional deformation modes [23]. However, even if the degradation products of these alloys, mainly Mg hydroxide and chloride, carbonates and phosphates, were found to be not dangerous and to naturally degrade within the body [24], a series of new formulations needs to be elaborated to optimize material performances and to overcome the issue of $H_{2(g)}$ formation, which is deleterious for the implant-surrounding tissues, as well as the high corrosion rate, about 0.49 ± 0.01 mm/year, found at the beginning of material–solution interactions [25–28]. Zn and its alloys have been the most recently studied biodegradable metals because of their interesting electrochemical behaviour. In fact, Zn has a standard corrosion potential of -0.76 V ($Zn^{2+} + 2e^- \leftrightarrow Zn_{(s)}$), intermediate between that of Fe, -0.44 V ($Fe^{2+} + 2e^- \leftrightarrow Fe_{(s)}$), and of Mg, -2.37 V ($Mg^{2+} + 2e^- \leftrightarrow Mg_{(s)}$), so that bioresorbable Zn and its alloys have a corrosion rate in the range of tens of micrometers per year, which is more acceptable than that of Mg- and Fe-ones [29]. Moreover, Zn alloys have attracted scientific interest because of their good cytocompatibility, lack of adverse toxic events, and absence of immune rejection [30]. However, the low mechanical properties of Zn means that this element, when used pure, is not directly suitable for biomedical applications, because a compromise between different properties is required for this purpose. Alloying with different elements allowed to increase the value of specific mechanical properties, especially for cardiovascular or orthopedic devices [31]. For this reason, the influence of different elements, such as Ag, Cu, Mg and Mn, on both mechanical properties and the corrosion behaviour of Zn was recently under deep investigation allowing to reach intermediate properties between those of Fe and Mg alloys [32]. For instance, the addition of Mg or Cu refines the microstructure and enhances yield strength and ultimate tensile strength proportional to the volume fraction of the secondary phases [33]. Element addition also brings to a wide range of measured corrosion rates, spanning from 0.188 ± 0.017 mm/year for Zn-3Ag-0.5Mg [34] to 0.044 ± 0.008 mm/year for Zn-5Cu [33]. These alloys, tested in commonly used physiological media, showed intergranular and micro-galvanic corrosion patterns, contributing to the formation of pits under the corrosion layer mainly due to the change of the electrochemical potential of the matrix grains by the dissolution of alloying elements and to the formation of micro-galvanic cells at the interface between the Zn-matrix and intermetallic phases [34–36]. Among the main outcomes, it was found that, independently from the corrosion media, Zn did not release $H_{2(g)}$ during biodegradation, contrarily to Mg, indicating one of its major benefits [37]. In addition, the metal displayed a uniform corrosion rate in SBF solution via immersion test and a homogenous distribution of corrosion products on the surface [38]. Degraded metal predominantly forms Zn oxide/hydroxide and Zn phosphate at the interface [38]. After testing high-purity Zn (99.99 wt.%) in SBF solution for 21 days, a layered structure made of four components was observed [39]. $ZnO/Zn(OH)_2$ was concentrated at the interface with the substrate while the Ca/P phase was found in the sub-internal and outermost layers, and Zn compounds, such as $Zn_3(PO_4)_2$, $Zn_5(OH)_8Cl_2$,

$Zn_5(CO_3)_2(OH)_6$ and $NaZn_4Cl(OH)_6SO_4 \cdot 6H_2O$, constituted the sub-external layer [39,40]. It was also proven that Zn phosphates, more than Zn oxides, increased cell viability, adhesion, and differentiation of pre-osteoblasts and vascular endothelial cells [41,42]. Besides improving cytocompatibility, the presence of $Zn_3(PO_4)_2$ showed antibacterial properties and a significant influence on controlling the metal corrosion behaviour [37]. In fact, the precipitation of phosphate-rich salts, HPO_4^{2-} and PO_4^{3-}, have been reported to enhance passivation and reduce the corrosion rate [43]. It is well known that, besides chemical composition and presence of second phases [44], the corrosion and degradation patterns of biodegradable alloys depend on other several variables, such as grain size [45], texture [11], thermomechanical treatments [46] and environmental factors, such as the atmosphere or the presence of salts or proteins in solution [47]. Moreover, the presence of specific anions, cations and molecules, like chloride ions, carbonates, phosphates and complex organic molecules, in pseudo-physiological solutions or in body environments, affect both in vivo and in vitro degradation. For this reason, different media are often used to test the degradation patterns of metallic alloys for biomedical applications. It must be noted that when devices are subjected to cardiovascular applications, they are also in contact with high CO_2 concentrations (5 vol.%) as they are immersed in the bloodstream [48]. For this reason, it is of great interest to study the influence of this specific parameter, CO_2 concentration, on the degradation pattern. This kind of study was conducted for an Fe-21Mn-1C alloy; in this case a specific degradation pattern and rate were found when 5 vol.% CO_2 was considered. A uniform and compact Mn carbonates degradation layer was observed while, under ambient condition, amorphous Fe phosphorous was predominant [49]. Despite some investigations on Zn degradation being conducted, its degradation mechanism and pattern in different media and atmospheres remain unclear [39]. For this reason, the works considering these effects on Zn degradation constitute an important preliminary step for further evaluations.

The present work investigates the effect of different pseudo-physiological solutions and atmospheres on the degradation of pure Zn. To simulate CO_2 amount in human blood, a 5 vol.% CO_2 atmosphere was selected. Static degradation immersion tests (SDIT) of 14 days were carried out on pure Zn immersed in three different solutions: Hanks' balanced salt solution (HBSS), Dulbecco's Phosphate-Buffered Saline (PSS) and sodium saline solution (NSS). Degraded surface chemistry and morphology were investigated with complementary characterization techniques to provide a reference for short-term degradation mechanisms of pure Zn, depending on the surrounding physiological media and atmosphere.

2. Materials and Methods

2.1. Samples Preparation

$20 \times 10 \times 1$ mm^3 coupons were obtained from commercial pure Zn (99.97 wt.%); they were cut from a rolled sheet, and a hole with a diameter $\varnothing = 1.4$ mm was drilled at a distance $d_1 = 5$ mm from the short edge, and at a distance $d_2 = 5$ mm from the long edge (Figure 1a). Samples were then polished with a series of abrasive papers up to 1200 grit to obtain a mirror-like surface. Polished samples were rinsed with water and ethanol, dried with compressed dry air, and then stored in a desiccator for further use. The chemical composition of the samples was studied and is shown in Table 1, which reports the chemical composition of polished Zn samples after more than 10 acquisitions by micro X-ray fluorescence (µXRF). The µXRF measurements were carried out with a Bruker Tornado M4, equipped with a Rh tube. The device was operated at V = 50 kV and A = 600 µA, with a spatial resolution of $s = 20$ µm and an acquisition time $t = 2$ ms. A residual pressure of P = 20 mbar was maintained in the measurement chamber. Samples were weighed before the test with a 5-digit precision digital balance (Analytical Plus, Ohaus, Parsippany, NJ, USA).
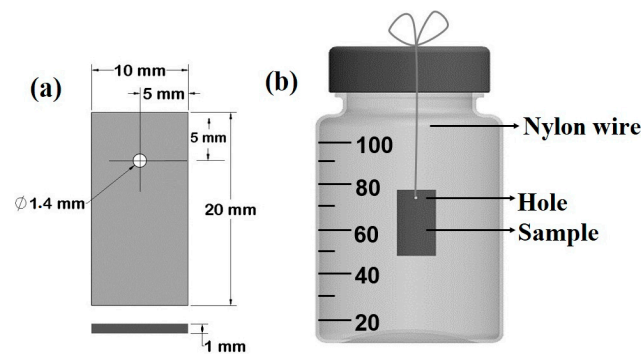
Figure 1. Schematic representation of testing sample (**a**) and of degradation test set-up (**b**).

Table 1. Actual composition (wt.%) of Zn samples.

Zn	Si	Al	Cu	Ti	Ni
Bal.	0.024(18)	0.0076(5)	0.0073(5)	0.0012(3)	0.0007(4)

2.2. Static Degradation Immersion Test (SDIT)

2.2.1. Solution Preparation

The test was conducted in a biological hood under sterile conditions. Sterilized 100 mL Pyrex bottles (Corning Incorporated; Corning, NY, USA 14831; Berlin, Germany) filled with the testing solutions were used and bottle caps drilled to ensure a proper gas exchange. Samples were suspended, using a nylon fishing line fixed on the top of cap hole, in the middle of the solution [50]. The volume of test solution was 95 ± 0.5 mL (Figure 1b).

The tests were carried out according to ASTMG31-12a [51]. The chosen media were three common pseudo-physiological solutions: (1) modified Hanks' salt solution (HSS); (2) a Dulbecco's phosphate-buffered saline solution (PSS); and (3) a physiological NaCl saline solution (NSS). HSS salt concentration is described in Table 2, as it is for the other media. This one was obtained from the dissolution in 1.4 L of nanopure water of a commercial bag of Hanks' solution (H1387, Sigma-Aldrich, St. Louis, MO, USA). The content of the bag was integrated with another set of salts (14.16 g of HEPES acid (H3375-5000G, Sigma-Aldrich. USA), 16.65 g of HEPES$^-$ Na$^+$ (H7006-500G. Sigma-Aldrich. USA) and 3.3 g of NaHCO$_3$ (S8875-500G, Sigma-Aldrich)), to produce a buffer. PSS was prepared by dissolving 9.6 g of salts (D5652, Sigma-Aldrich) in 1 L of nanopure water; NSS was achieved by dissolving 8.94 g of NaCl (S5886-1Kg, Sigma-Aldrich) in 1 L of nanopure water. The pH of the three solutions was adjusted to 7.4, using 1 M NaOH or 1 M HCl aqueous solutions.

Table 2. Inorganic salts used for the three solutions. The quantity is expressed in g per L. One L of deionized water was used for each preparation.

	Modified Hanks' Solution	Phosphate-Buffered Solution	Sodium Chloride Solution
CaCl$_2$·H$_2$O	0.13	-	-
MgSO$_4$	0.07	-	-
KCl	0.29	0.20	-
KH$_2$PO$_4$	0.04	0.20	-
Na$_2$HPO	0.03	1.15	-
NaCl	5.71	8.0	8.94
α-D-Glucose	0.71	-	-
NaHCO$_3$	0.25	-	-
HEPES acid	10.11	-	-
HEPES sodium salt	11.89	-	-

After the preparation, solutions were subjected to filtration through a disposable filtration system (Steritop®, SCGPS02RE, EMD Millipore, Burlington, MA, USA). The operation was carried out under a sterile biological hood.

2.2.2. Specimen Immersion

Filtered solutions were then used, filling 5 bottles for conditions with the appropriate amount of solution and a specimen. Each bottle was incubated for 14 days either (a) in an incubator with 5 vol.% CO_2 (T = 37 ± 1 °C, relative humidity RH = 85%), or (b) in ambient atmosphere containing 0.04 vol.% CO_2 (T = 37 ± 1 °C; HR = 100%). In addition, for clarity, conditions (a) and (b) are referred to as "X_{air}" or "X_{CO2}", where X = HSS, PSS, NSS, while "air" or "CO_2" are related to the used atmosphere, that is either lower or higher CO_2 concentration, respectively. For example, according to this denomination system, a Zn sample tested in HSS in a CO_2 rich atmosphere would be named as Zn_{HSS_CO2}. Zn samples before immersion were also characterized and referred to as Zn_{BASE} (Table 3).

Table 3. Sample acronyms as function of the experimental conditions used for degradation tests.

Sample Acronym	Solution Acronym	Atmosphere
Zn_{BASE}	-	-
Zn_{HSS_air}	HSS_{air}	air (low-CO_2)
Zn_{HSS_CO2}	HSS_{CO2}	incubator (high-CO_2)
Zn_{PSS_air}	PSS_{air}	air (low-CO_2)
Zn_{PSS_CO2}	PSS_{CO2}	incubator (high-CO_2)
Zn_{NSS_air}	NSS_{air}	air (low-CO_2)
Zn_{NSS_CO2}	NSS_{CO2}	incubator (high-CO_2)

The minimum "solution volume-to-specimen area" ratio was 0.40 mL/mm^2, according to ASTM G31.

2.2.3. Sample Extraction and Waste Solution Management

Once the duration of time had expired, the specimens were extracted, ultrasonically cleaned in 70 vol.% ethanol solution for 5 min, and finally weighed three times. After each cleaning, the sample weight loss was compared with the preceding one; the process was repeated until two succeeding weighings did not show a weight difference higher than 1 mg, or after a maximum of three weighings. Subsequently, the cleaned samples were stored in a desiccator at room temperature until they were characterized. The corrosion rate (*CR*) was determined following the protocol established by ASTM G31-21. This standard procedure recommends the use of the following parameters: the time of exposure (*t*) to the medium in hours, surface area of sample (*A*) in cm^2, in contact with solution, mass loss (*W*) in grams and sample density (ρ) in g/cm^3, as described in Equation (1):

$$CR = \frac{8.76 \times 10^4\, W}{At\rho} \tag{1}$$

The waste media for each sample were collected after the test; they were centrifuged (Marshall scientific. Beckman Allegra 6R, Hampton, NH, USA) for 45 min (15 min × 3) at 4000 rpm, to separate the precipitates (degradation products) from the supernatant. The supernatant was digested to quantify the concentration of Zn ion in the solution.

2.2.4. Sample Digestion and Zn Solubility Assessment

Briefly, 3 mL of supernatant were put in a scintillation vial and heated in a silicone oil bath to a temperature of 90 °C. After this, 3 mL HNO_3 (CA 87003-261, VWR Aristar plus) was added to each vial and the temperature adjusted to 115 °C evaporating the solution

until 3 mL. Next, 600 μL of nanopure water and 900 μL of 30 vol.% H_2O_2 were added and re-heated at the same temperature of 115 °C. Finally, 7 mL of 1 vol.% HNO_3 solution was added to the resulting solution to add up to a total volume of 10 mL, followed by Zn ion release analysis using microwave plasma-atomic emission spectrometry (MP-AES; Model 4200, Agilent equipment).

2.3. Samples Characterization

Each samples characterization was conducted before and after 14 days of exposure to the three pseudo-physiological solutions. Different kinds of complementary characterization techniques were used and the related details about instruments and experimental parameters are reported in Table 4. Surface morphology and the structure of phases were assessed by scanning electron microscopy coupled with energy dispersive spectroscopy system and X-ray diffraction, respectively. Chemical groups involved in degraded products attached to Zn surfaces were analyzed using attenuated total reflection-Fourier transform infrared spectroscope. A background measurement with 64 scans, utilizing a white silicone crystal, prior to FTIR measurements at a range of 4000–400 cm^{-1} and with a resolution of 4 cm^{-1}, was carried out. Chemical composition of degraded surfaces was analyzed by X-ray photoelectron spectroscopy. A survey spectrum covering the range of 0–1400 eV was first recorded using a standard achromatic Al K$_\alpha$ X-ray source (1488.6 eV) at 200 W. Spectra deconvolution then was performed using PHI MultiPak™ software (version 9.1) and Gaussian–Lorentz functions with a Shirley background. A total of three acquisitions were performed for each condition.

Table 4. Characterization techniques used in the work: details of instruments and related operating parameters.

Characterization Technique	Instrument	Experimental Details
Surface morphology and composition		
Scanning Electron Microscopy (SEM)	Model: FEI, Quanta 250, Japan	W filament source; acceleration voltage (10–15 kV); spot size (3.0–6.0)
Energy Dispersive Spectroscopy (EDS) system	Model: AMETEK.	EDS system includes Octane Pro detector for elemental analysis
Structure and crystallinity of phases		
X-ray diffraction (XRD)	Model: D5000 SIEMENS system ($\lambda_{\text{Cu K}\alpha}$ = 1.5418 Å)	2θ scanning angle in the range of 6–120°; Scan rate = 0.1°/min; step time = 2 s/°; anode current: 50 mA; accelerated voltage = 40 kV using graphite monochromator
Chemical groups and composition		
Attenuated total reflection-Fourier transform infrared spectroscope (ATR-FTIR)	Model: Agilent Cary 660 FTIR, Agilent Technologies, Minnetonka, MN, USA	Deuterated L-alanine doped triglycine sulphate (DLa-TGS) detector; Ge coated KBr beam splitter
X-ray photoelectron spectroscopy (XPS)	Model: Physical Electronics PHI 5600-ci spectrometer (Chanhassen; MN; USA)	Spectrometer operating with an incident angle of 45° and a residual pressure of 3 × 10^{-9} Torr. Standard achromatic Al K$_\alpha$ X-ray source (1488.6 eV)

3. Results

3.1. SEM-EDS Analysis

SEM-EDS analysis was conducted on both corroded surface and degradation products attached to the corroded surface of each sample. It should be noted that, for each sample, the figures showing degradations products are representative of the degradation products that are close to the hole of the testing sample, where degradation product accumulation

generally occurred mainly due to gravity reasons (Figures 2, 3 and 4c,f). Figure 2a–c show SEM micrographs for Zn_{HSS_air} and Zn_{HSS_CO2} samples. A flat and compact degradation product layer extended on the degraded Zn_{HSS_air} surface, characterized by precipitates of white patches homogenously distributed and by sparse holes of different dimensions, presumably due to a localized corrosion of the bare metal. Elemental analysis of these cavities revealed the presence of Zn, O and P (point B in Figure 2g), while that of the degradation products revealed mainly Zn and O (point C in Figure 2c); this could be consistent with the presence of Zn and ZnO evidenced by XRD (Figure 5), as well as phosphates, found mainly in the FTIR spectrum (Figure 6). Similarly to the HSS_{air} condition, degradation products for the HSS_{CO2} condition appeared to form quite a smooth passivation base layer and, on the top of it, globular white degradation products forming aggregates, more or less of the same size, spread all over the surface (Figure 2e,f). EDS analyses were performed on the two different features of the degraded surface for Zn_{HSS_CO2}: this evidenced the presence of Zn and O both for the smooth base layer (point G2) and for the surface clusters (points E and G1). However, only traces of P and Ca were found for the point G2, while consistent amounts of the same elements were found for the points E and G1. The results obtained are consistent with the presence of Zn and ZnO, detected by XRD (Figure 5), and of phosphate groups, PO_4^{3-}, found during FTIR analysis (Figure 6). Watroba et al. [34] also evaluated degradation of pure Zn in Hanks' solution for 14 days, under ambient atmosphere. They found that the specimen surface was covered with a compact corrosion layer, on which another kind of degradation product was dispersed uniformly; even in this case, the dispersed cluster had the shape of white globular aggregates. Two other recent studies [39,40] confirmed a similar morphology for degraded samples, especially for Zn samples tested in the same condition when immersed in SBF solution. In the present study, degraded surfaces of Zn_{HSS_CO2} samples presented white clusters of significantly bigger size than those present on the surface of Zn_{HSS_air}.
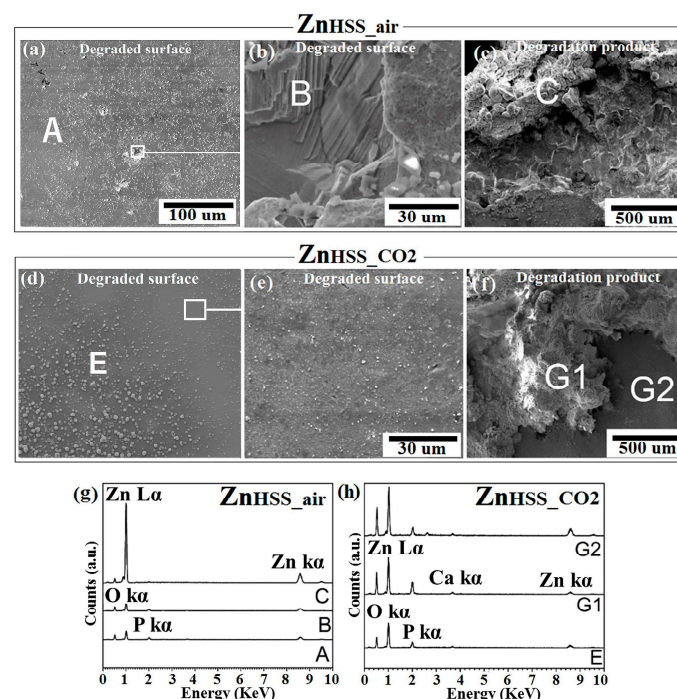

Figure 2. SEM analysis of Zn samples after 14-day immersion in modified Hanks' solution under ambient atmosphere (HSS_{air}) and incubation (HSS_{CO2}), respectively: corroded surface (**a**,**d**) and the related higher magnification (**b**,**e**); degradation product (**c**,**f**). EDS analysis of points A, B, C of Zn_{HSS_air} (**g**); points E, G1, G2 of Zn_{HSS_CO2} (**h**).

Contrarily to the generally compact degradation layer composed of Zn oxide and phosphates, observed for both Zn_{HSS_air} and Zn_{HSS_CO2}, the corroded surface of Zn_{PSS_air}

appeared to be covered by patches of crystallized degradation products (Figure 3a,b). SEM micrographs also showed cracks and delimiting adjacent segments of the crystallized degradation product layer (Figure 3c). Another surface morphology could be found on the degraded surface, showing a bare (as confirmed by XRD) corroded underlayer: in this case, the surface conformation seemed to put in evidence the grain microstructure of the base material, with corrosion features aligned along specific directions varying form grain to grain. These could be attributed to the different orientation of each grain. The general surface features for Zn_{PBS_air} and Zn_{PBS_CO2} appeared to be similar and composed by a well-crystallized layer superposed to a corroded metallic substrate. Figure 3g reports the elemental analysis of the degradation product layer, evidencing the presence of Zn, O and P (point B of Figure 3b,c), while the underlying surface (point A of Figure 3a) showed mainly pure Zn (Figure 3g). A similar trend was observed for Zn_{PSS_CO2}, with minor differences if compared with Zn_{PSS_air}; for example, more relevant cracks were present around the degradation product segments, and a less regular growth of the degradation layer, compared to what was already seen for Zn_{PSS_air} (Figure 3d–f). Figure 3h shows the chemical composition of the regular hexagonal degradation products, mainly formed of Zn, O and P (points E, G of Figure 3d,f), while the corroded metallic surface substrate (point F in Figure 3e) showed mainly the presence of Zn (Figure 3h). Both RX and FTIR analysis of Zn_{PSS_air} and Zn_{PSS_CO2} are in good agreement with these findings (Figures 5 and 6). In 2016, Chen et al. [52] studied Zn degradation in PBS solution, observing the presence of two distinct kinds of surface morphologies; that is a pebble-like uniformly corroded one, and a non-uniform localized corroded one, both after 3- and 7-days of immersion. These authors increased immersion time up to 21 days, and corrosion products on the degraded surface appeared to show a relatively coarse shingle-like morphology on the whole surface. The morphology of degradation products in the first degradation steps was confirmed with this study; moreover, a layer composed of higher-dimensions degradation product crystals was here found when a high CO_2 content atmosphere was considered (Figure 3c,f).
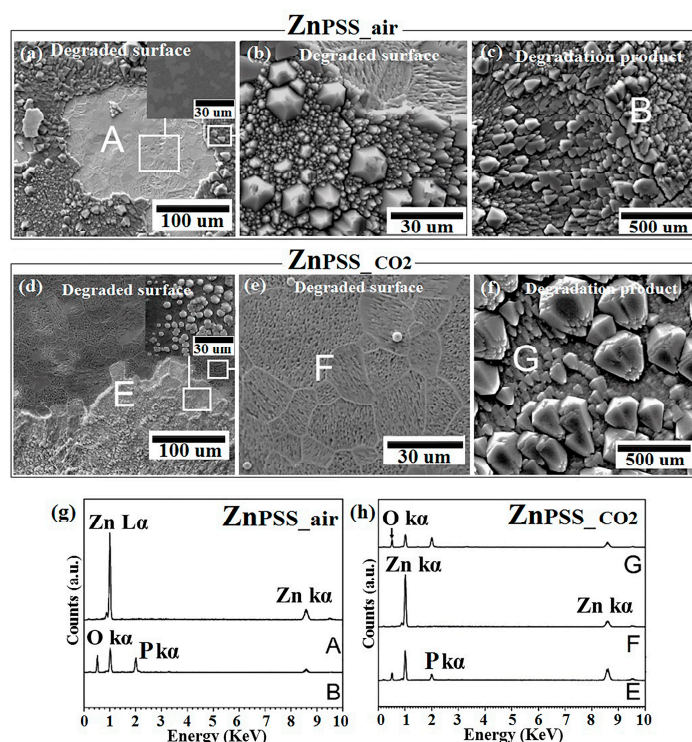

Figure 3. SEM analysis of Zn samples after 14-day immersion in phosphate-buffered solution under ambient atmosphere (PSS_{air}) and incubation (PSS_{CO2}), respectively: corroded surface (**a,d**) and the related higher magnification (**b,e**); degradation product (**c,f**). EDS analysis of points A, B of Zn_{PSS_air} (**g**); points E, F, G of Zn_{PSS_CO2} (**h**).

For Zn_{NSS_air}-degraded surface a high density of cavities could be observed, presumably due to a higher corrosion rate, taking place in a non-uniform way (Figure 4a). As previously reported [53], the corrosion rate of pure Zn was severely high in an ambient environment, ostensibly due to the action of a high amount of chlorine ions, leading to a preferential etching of grain boundaries. The Zn_{NSS_CO2} sample showed a lower number of cavities and a less aggressive boundaries etching, corresponding to a more homogenous corrosion, while O- and Zn-rich aggregates were detected on the surface (point F1, Figure 4e). Chemical analysis by EDS evidenced, in fact, the presence mainly of Zn and O for all of the tested areas of Zn_{NSS_CO2} while bare metal was found in some analysed points of Zn_{NSS_air} (A1, A2 of Figure 4g). Cl is barely visible in EDS spectra but the presence of $ZnCl_2$ was detected by XR and FTIR analyses conducted on both Zn_{NSS_air} and Zn_{NSS_CO2}-degraded surfaces. Morphology found for Zn_{NSS_air} samples was very similar to that reported by Zou et al. [54], for Zn tested in a similar condition. In the present study, the topmost layer showed a loosely attached film of degradation products. This was specifically found for Zn_{NSS_air} (Figure 4b). For this same NSS solution, the layers constituting the Zn samples tested in the CO_2-rich condition revealed a more homogenous surface morphology (Figure 4d), while a clear grain boundaries attack was found for both atmospheres (Figure 4b,e).
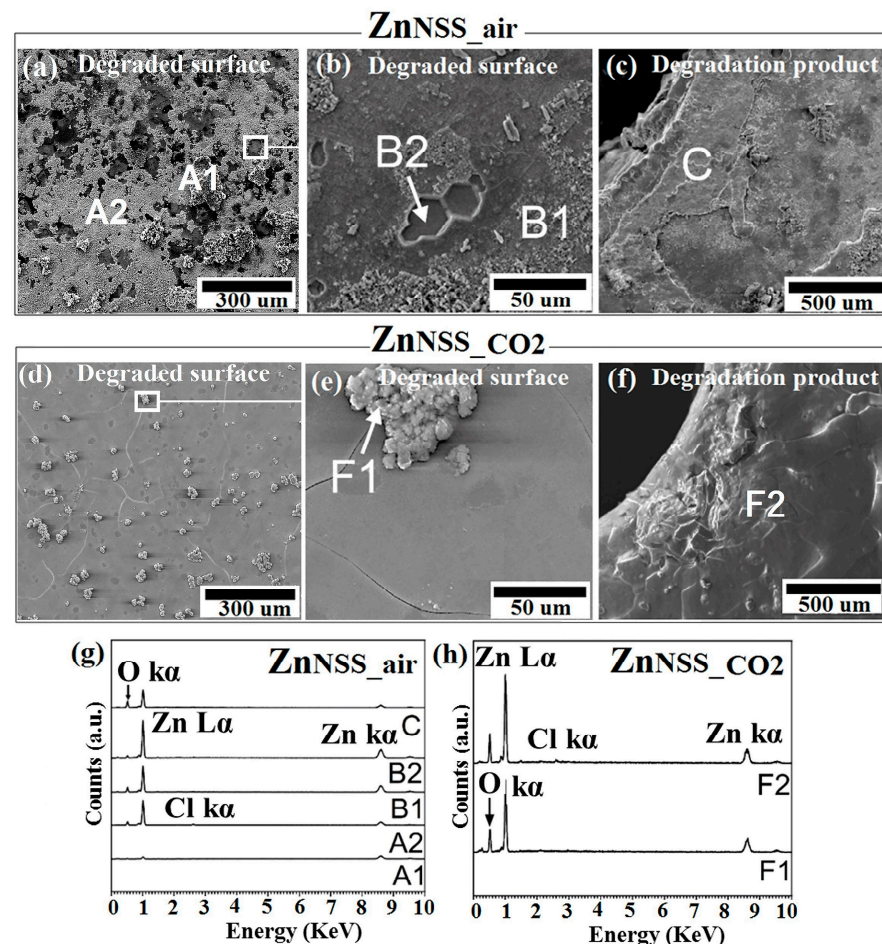

Figure 4. SEM analysis of Zn samples after 14-day immersion in sodium chloride solution under ambient atmosphere (NSS_{air}) and incubation (NSS_{CO2}), respectively: corroded surface (**a**,**d**) and the related higher magnifications (**b**,**e**); degradation products (**c**,**f**). EDS analysis of points and A1, A2, B1, B2, C of Zn_{PSS_air} (**g**); points F1, F2 of Zn_{PSS_CO2} (**h**).
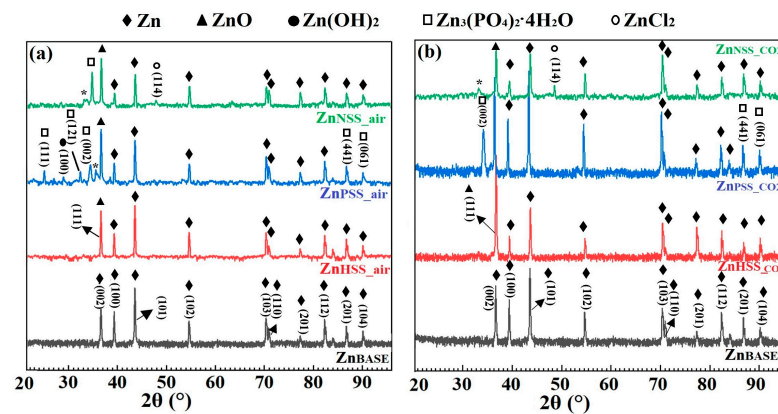
Figure 5. Indexed XRD diffraction patterns of Zn sample before immersion (Zn_{BASE}) and after 14-day immersion in the three solutions at low CO_2 content atmosphere (**a**) and at high-CO_2 content atmosphere (**b**).
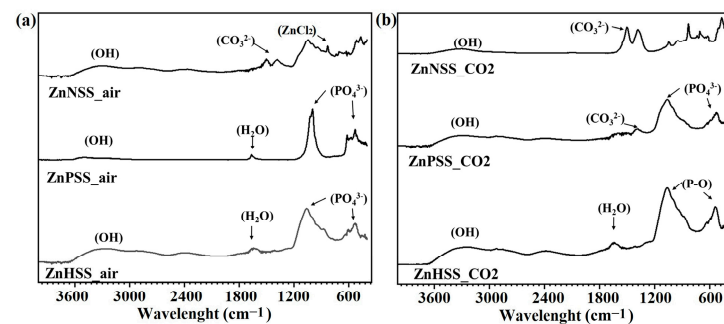

Figure 6. FTIR analysis of Zn_{HSS_air}, Zn_{PSS_air}, Zn_{NSS_air} (**a**) and Zn_{HSS_CO2}, Zn_{PSS_CO2} and Zn_{NSS_CO2} (**b**).

3.2. XRD Analysis

Similar XRD patterns were observed for both CO_2 and ambient atmospheric conditions (Figure 5a,b).

XRD spectra for Zn before immersion, the Zn_{BASE} sample, showed the presence of a series of peaks corresponding to Zn, characterized by a hexagonal compact crystalline structure, with prominent 2θ peaks at 36.82° corresponding to the (002) plane, 39.29° to (100), 43.78° to (101), 54.55° to (102), 70.54° to (103) and 70.94° to (110) [55]. Other smaller peaks, respectively at (112), (201) and (104) planes, and corresponding to Zn, are visible at higher 2θ. Other phases with XRD peaks attributable to ZnO, $ZnCl_2$, $Zn(OH)_2$ and $Zn_3(PO_4)_2·4H_2O$ (α-hopeite) could be observed for samples immersed in pseudo-physiological solutions. A peak corresponding to the (111) reflexion plane, attributable to ZnO [56], was observed for all the immersed samples while three major peaks corresponding to (002), (413) and (061), attributed to α-hopeite [57], were found for both Zn_{PSS_air} and Zn_{PSS_CO2}. These finding corroborated both EDS and FTIR characterizations of the same samples; in fact, the presence of Zn, O, P and of PO_4^{3-} groups, respectively, was detected. Moreover, a well-visible crystallized layer of degradation products was observed from SEM images (Figure 3) confirming the presence of crystallized phosphates found by XR. Three no-indexed small peaks were found in the spectra of Zn_{PSS_air} and Zn_{NSS_CO2} samples and identified with a star (*); they are related to complex phases which are phosphate- and chloride-based, respectively, for which a clear identification was not reached. For HSS samples no peaks of phosphates were detected by XR analysis so that the presence of phosphates observed by EDS and FTIR make one think about the formation of amorphous phosphates. A peak corresponding to the (002) reflexion plane [58], attributable to $Zn(OH)_2$, was distinguishable just for Zn_{HSS_air}. A peak corresponding to the (114) reflexion plane, attributable to $ZnCl_2$ [59], was found just for samples tested in NSS solution independently

from the atmosphere and this result was confirmed by FTIR analysis. While $ZnCl_2$ was found only on the surface of Zn samples immersed in NSS solutions, on the other hand, peaks corresponding to (111) for ZnO were found for all of the samples tested in the different media.

3.3. FTIR Analysis

The broad peaks in the high-wave-number region 3600–2900 cm^{-1} could be ascribed to the presence of -OH groups. The sharp peaks in the low-frequency regions and corresponding to the positions of 1040 and 516 cm^{-1}, could be attributed to P-O asymmetric stretching vibration of phosphate, PO_4^{3-} [40,60,61]. Furthermore, the peak at 868 cm^{-1} was indicative of the presence of Zn-Cl [62]. $ZnCl_2$ was mainly observed for Zn_{NSS_air} and Zn_{NSS_CO2}, showing the formation of Cl-containing compounds on the surface of samples immersed in NSS. Additionally, peaks in the mid-frequency regions, such as those at 1640 and 1160 cm^{-1} and at 1500 and 1380 cm^{-1}, could be assigned to H_2O bending, P-O bonding and presence of carbonates, respectively [40,63]. Since no peaks of carbonates were found by XRD analysis, it can be assumed that carbonate peaks, mainly found for Zn samples immersed in both PSS and NSS under a CO_2-rich atmosphere and confirmed by XPS analysis, belong to degradation products showing an amorphous form.

The presence of strong peaks such as those corresponding to phosphate ($H_2PO_4^-$, HPO_4^2, PO_4^{3-}) and carbonate (HCO_3^-, CO_3^{2-}) groups could be attributed to the presence of the corresponding ions in HSS and PSS solutions [64,65]. The formation of carbonates, influenced by CO_2 concentration (Figure 6b), was identified, in fact, for Zn_{PSS_CO2} and Zn_{NSS_CO2}. Weaker carbonate-related peaks were also found for Zn_{HSS_CO2}, which were attributed to the effects of a higher CO_2 atmospheric pressure. The presence of carbonate-related species could also be found for Zn_{NSS_air}, probably due to the corrosive effect of Cl^- ions, and to the low K_{sp} for $ZnCO_3$ [66,67]. The different characterization techniques confirmed the formation of a series of degradation products, for example $Zn_3(PO_4)_2$, $ZnCO_3$, oxides, hydroxides and $ZnCl_2$, specifically for sample exposition for NSS solution.

3.4. XPS Analysis

The amount of C, O and Zn as well as traces of Na, Ca, Cl and P in the Zn_{BASE} sample and for all the other conditions was detected by XPS and reported in Figure 7a,b. Results showed some differences for the different atmosphere condition. C ranged from 36.47 ± 1.86 to 24.1 ± 7.01 at.% for samples immersed in a low CO_2 atmosphere, while from 30.50 ± 2.66 to 13.47 ± 3.18 at.% for high CO_2 content solutions. As it was possible to see from high-resolution spectra, a consistent amount of C could be attributed to the presence of adventitious carbon [68]. Similarly, O ranged from 49.13 ± 3.76 to 43.53 ± 0.45 at.% for the low CO_2 condition, while from 54.10 ± 2.79 to 47.66 ± 1.54 at.% for the high CO_2 one. As expected, Zn content was almost the same for both conditions, from 29.20 ± 0.44 to 10.66 ± 1.76 at.%. The surface amount of Zn was generally higher for NSS.
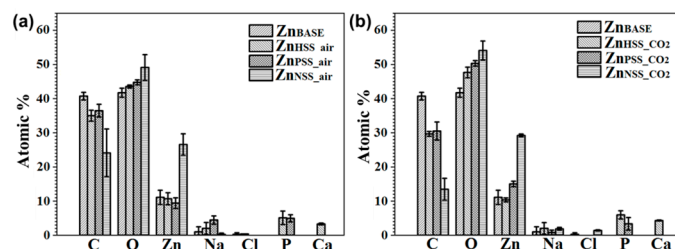

Figure 7. XPS survey of Zn samples before immersion and after 14-day immersion in the tested three solutions under ambient atmosphere (**a**) and CO_2-rich atmosphere (**b**), respectively.

For clarity, only high-resolution spectra of C1s, O1s and Zn2p$_3$ for Zn_{BASE} and samples immersed in HSS_{air} and HSS_{CO2} solutions are presented here, being representative of the other conditions. Information about high-resolution spectra of other conditions are

reported in Figures S1–S4 of the Supplementary data section. Figure 8a–c reveal similar deconvolutions for all tested conditions.
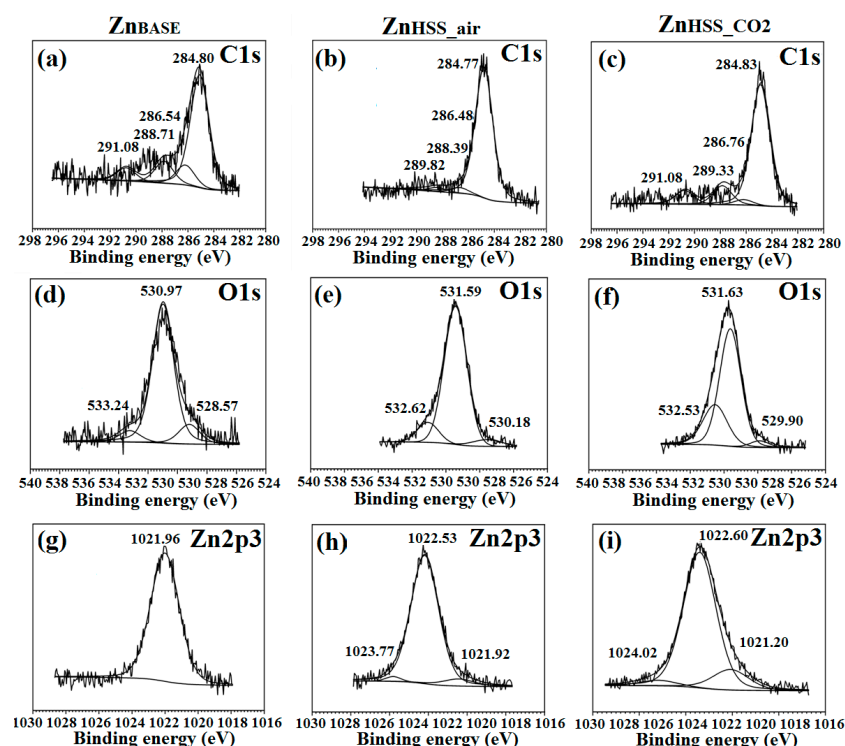

Figure 8. XPS High-resolution of C1s (**a**–**c**), O1s (**d**–**f**) and $Zn2p_{3/2}$ (**g**–**i**) for Zn_{BASE}, Zn_{HSS_air} and Zn_{HSS_CO2}, respectively.

The carbon C1s peaks at ~284.8 eV, ~286.4 eV and ~288.5 eV could be attributed to C–C and C–H_2, –C–OH and –O–C=O binding energies, respectively [50]. The presence of a fourth peak at ~291.08 eV, observed for Zn_{HSS_CO2}, represents an indication of possible trapping of CO_2 and formation of carbonates as degradation products [10]. Evidently, the peak area under 284.8 eV significantly increased for Zn_{HSS_CO2} compared to Zn_{HSS_air} (Table 4). O1s energy bands were deconvoluted in three contributions: the first one was found in the range 528.6–530.2 eV and attributed to the presence of O directly bound to the metal, Me–O, and responsible for the formation of ZnO [69]. The second one, found between 531.0–531.7 eV, was attributed to the presence of hydroxide groups and O linked to C, –OH and O–C. The third band, in the range 532.6–533.4 eV, was attributed to the presence of adsorbed water on the sample surface [70]. The peak found in the Zn $2p_{3/2}$ spectra, centered at about 1022 eV, could be attributed to various oxidized Zn states, mainly ZnO and Zn [39,70]. The deconvolution binding energy peak located at 1024.02 eV for Zn_{HSS_CO2} was proposed as evidence of the presence of zinc phosphate species, while for a lower bonding energy 1021.2 eV could be attributed to the presence of ZnO or $Zn(OH)_2$ species [71]. The deconvolution of C, P, O and Zn energy bands for Zn_{PSS_air} and Zn_{PSS_CO2}, present in the Supplementary material section, could be attributed to the formation of mixed Zn phosphates and carbonates [39] while energy bands related to phosphates for Zn_{NSS} and Zn_{BASE} samples were not present.

3.5. Corrosion Rate

The corrosion rates calculated for the different conditions varied significantly (Figure 9a). In modified Hanks' solution and under a 5 vol.% CO_2 atmosphere, the *CR* was generally CR_{HSS_CO2} = 0.02 ± 0.01 mm/year. This value could be compared to CR_{HSS_air} = 0.06 ± 0.03 mm/year, higher than the previously mentioned one, and similar to those reported in the literature [33,34,40]. For PSS immersion, an opposite trend was found; in

fact, $CR_{PSS\_CO2} = 0.14 \pm 0.02$ mm/year was higher than $CR_{PSS\_air} = 0.03 \pm 0.008$ mm/year. The corrosion rate was relatively high under both CO_2 and atmospheric conditions for samples immersed in NSS, probably due to Cl ion attack [59]. $CR = 0.13 \pm 0.01$ mm/year and the $CR = 0.20 \pm 0.07$ mm/year were achieved for Zn_{NSS_CO2} and Zn_{NSS_air}, respectively. The high CR for Zn_{PSS_CO2}, despite the formation of a degradation passivation layer, was attributed to possibly higher corrosion kinetics as a result of micro-galvanic coupling between the metal and its degradation products [34]. To further investigate Zn ion release mechanism, MP-AES was performed (Figure 9b). In general, the Zn release rate for ambient conditions was lower than in a CO_2-rich atmosphere, or at least of the same amount, for PSS exposition. High A Zn ion release rate for a CO_2-rich atmosphere presumably led to the formation of carbonate degradation products. A Zn ion release of 0.52 ± 0.15 mg/L was observed for Zn_{HSS_air} compared to 1.70 ± 0.85 mg/L for Zn_{HSS_CO2}. Significantly higher ion releases were observed for samples immersed in NSS solution and, also in this case, Zn ion release was much higher when a CO_2-rich atmosphere was used.
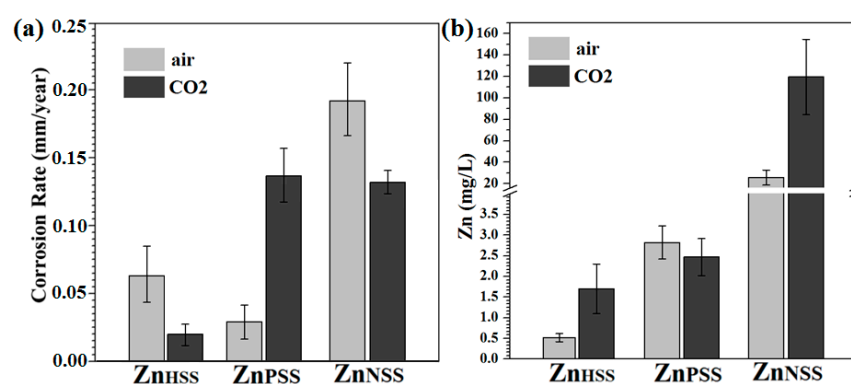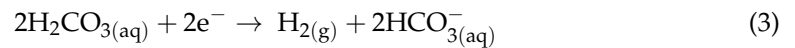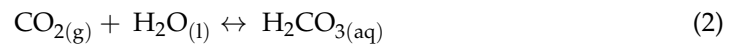

Figure 9. Corrosion rate (**a**) and Zn ion release rate (**b**) of Zn samples after 14-day immersion in modified Hanks' solution (HSS), phosphate-buffered saline (PSS) and saline solution (NSS) under CO_2 atmosphere and ambient air conditions.

4. Discussion

Body fluids are aqueous solutions consisting of organic compounds, proteins, bicarbonates, phosphates, chlorides and aggressive ions, which undergo complex interactions with metallic biodegradable surfaces producing different kinds of degradation products [62]. Thus, the composition of the pseudo-physiological fluid, the considered atmosphere (CO_2-rich or CO_2-poor), among others, can significantly affect in vitro and in vivo behaviour of biodegradable metals. As is known, Henry's Law reports that the CO_2 amount dissolved in a liquid is proportional to the partial pressure of the gas [72]. The two studied atmospheres, 0.04 and 5 vol.% CO_2, were selected to simulate reference values for ambient conditions and the human arteriosus blood atmosphere, respectively. Considering the solubility coefficient of CO_2, $S(CO_2) = 0.0309$ [mM/Torr] [49], it is possible to estimate the concentration of the gas in air, 9.75×10^{-2} mM, and in a 5 vol.% CO_2 condition, 11.742 mM, and from the latter, the concentration of CO_2 in arteriosus blood, 40 mM [49]. The selected CO_2-rich atmosphere of this study is of interest because it is comparable with the amount of CO_2 present in the human circulatory system, even if lower. In the work of Mouzou et al. [11], the presence of 5 vol.% CO_2 led to the formation of carbonates of different chemical stabilities significantly affecting the corrosion behavior of Fe-21Mn-1C whose CR was six times lower when a testing atmosphere with 5 vol.% of CO_2 was considered. While some results on Zn-based materials' degradation in Hanks' solution or SBF were reported [39], works on the degradation of Zn and formation of degradation products in a pseudo-physiological fluid with a CO_2-rich atmosphere are still missing. Most CO_2 molecules dissolved in the blood plasma are carried as part of the bicarbonate-buffered system which allows the conversion of the gas into carbonic acid, H_2CO_3. The latter constitutes an intermediate molecule that immediately forms HCO^{3-} and H^+ ions. HCO_3^- acts as a pH buffer allowing nutrient

and metabolite fluctuations without causing important pH changes [48] According to that, CO_2 dissolves in water forming carbonic acid and HCO_3^- and CO_3^{2-} anions, as indicated by Equations (2)–(4):
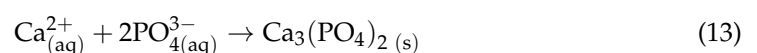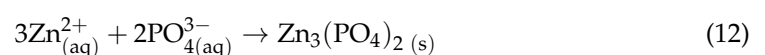
$$CO_{2(g)} + H_2O_{(l)} \leftrightarrow H_2CO_{3(aq)} \tag{2}$$

$$2H_2CO_{3(aq)} + 2e^- \rightarrow H_{2(g)} + 2HCO_{3(aq)}^- \tag{3}$$

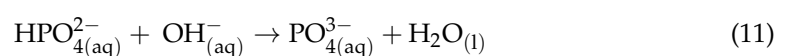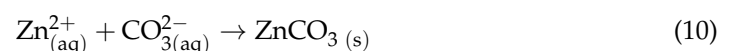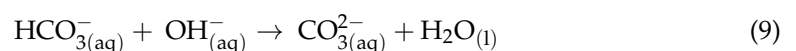$$2HCO_{3(aq)}^- + 2e^- \rightarrow H_{2(g)} + 2CO_{3(aq)}^{2-} \tag{4}$$

A higher CO_2 amount brings to a higher anion amount so that the difference in HCO_3^- and CO_3^{2-} concentrations of the two atmospheres had an influence on the aspect of carbonates passivating layers formed under different testing conditions, as visible from SEM analysis (Figures 2–4). However, the *CR* of Zn samples was not as different as that found for the Fe-21Mn-1C alloy tested under ambient and 5 vol.% CO_2 conditions, respectively [11]. In fact, for all Zn samples a starting mixed Zn oxide/hydroxide layer was found. The degradation mechanism of pure Zn in different pseudo-physiological solutions starts, in general and for the specific case, with the following anodic and cathodic reactions, generating metal ions and $H_{2(g)}$:

$$Zn_{(s)} \rightarrow Zn_{(aq)}^{2+} + 2e^- \tag{5}$$

$$2H_2O_{(l)} + 2e^- \rightarrow 2OH_{(aq)}^- + H_{2\,(g)} \tag{6}$$
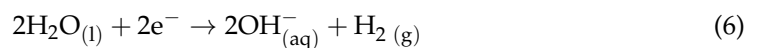
According to Pourbaix diagram of Zn, the presence of OH^- ions in the media results in an increased solution pH and, consequently, in the formation of $Zn(OH)_2$ and its dehydration product, ZnO [1,39,53]:

$$Zn_{(aq)}^{2+} + 2OH_{(aq)}^- \rightarrow Zn(OH)_{2\,(s)} \tag{7}$$

$$Zn(OH)_{2\,(s)} \rightarrow ZnO_{(s)} + 2H_2O_{(l)} \tag{8}$$
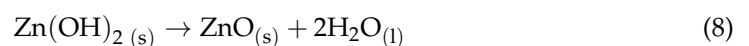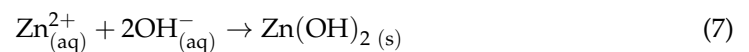
A mixed layer composed of ZnO, $Zn(OH)_2$, and other compounds was detected by XRD, XPS and FTIR analysis for samples tested in HSS and PSS. Even if $Zn(OH)_2$ was not found with the different techniques, it is reasonable its formation was an intermediate corrosion product [40]. Note that the effect of degradation products on metal degradation can be twofold: they can accelerate the corrosion process due to the formation of the micro-galvanic cells with Zn, while the promoted formation of Zn oxide, carbonates and phosphates may inhibit the degradation process of the substrate [34]. Thus, the formation of HCO_3^-, CO_3^{2-}, HPO_4^{2-} and PO_4^{3-} anions depends on different variables such as pH, temperature and, in our case, CO_2 content [73].

$$HCO_{3(aq)}^- + OH_{(aq)}^- \rightarrow CO_{3(aq)}^{2-} + H_2O_{(l)} \tag{9}$$

$$Zn_{(aq)}^{2+} + CO_{3(aq)}^{2-} \rightarrow ZnCO_{3\,(s)} \tag{10}$$

$$HPO_{4(aq)}^{2-} + OH_{(aq)}^- \rightarrow PO_{4(aq)}^{3-} + H_2O_{(l)} \tag{11}$$

$$3Zn_{(aq)}^{2+} + 2PO_{4(aq)}^{3-} \rightarrow Zn_3(PO_4)_{2\,(s)} \tag{12}$$

$$Ca_{(aq)}^{2+} + 2PO_{4(aq)}^{3-} \rightarrow Ca_3(PO_4)_{2\,(s)} \tag{13}$$

$$Ca^{2+}_{(aq)} + 2HPO^{2-}_{4(aq)} + H_2O_{(l)} \rightarrow CaHPO_4 \cdot 2H_2O \tag{14}$$

The corrosion rate of pure Zn was generally lower in CO_2-rich atmosphere compared to ambient conditions, particularly for HSS and NSS (Figure 9a) and Zn ion release was higher (Figure 9b), which promotes formation of carbonates and phosphates in the passive layer from reaction of CO_2 with the excess of metallic ions. For samples tested in HSS, a more compact layer of spherical precipitates was observed when a CO_2-rich atmosphere was considered. Patches of hexagonal sharp-edges cavities were bigger for ZnP_{SS_CO2} samples and less cavities were found on the Zn_{NSS_CO2} surface. These features influenced the corrosion rate that, for samples tested in air, was about two times higher for both HSS and NSS solutions. Contrarily, the *CR* was significantly lower for samples tested in air when PSS solution was considered. It should be noted that the high corrosion rate for Zn_{PSS_CO2}, despite the formation of a compact passivating degradation layer, is due to the presence of zones where there is delamination of the passivation layer; this could lead to an acceleration of the corrosion rate, as a result of local galvanic coupling, until all of the surface is covered. The concentration of Zn ion released in the waste solution was significantly higher for samples immersed in NSS solution reaching the highest values for Zn_{NSS_CO2} (Figure 9b). This can be attributed to the important presence of chloride ions in NSS solution, playing an important role in promoting the corrosion rate. It is reported that while the corrosion-passivating layer provides protection, defects in the corrosion-passivating layer partly facilitate Cl^- ion permeation, leading to a gradual increase in Cl^- ion concentration, acidification of the microenvironment (or local acidification) and delamination of degradation layers [34]. In fact, the significant presence of Cl^- ions in both NSS solutions can lead to an evident delamination of its degradation products layer increasing the corrosion rate in such a microenvironment [34,59] (Figures 4 and 9). Thus, the highest corrosion rate obtained for Zn_{NSS_CO2} and Zn_{NSS_air}, which is 0.13 ± 0.01 and 0.20 ± 0.07 mm/years, respectively, can be attributed to Cl^- ion presence in addition to micro-galvanic coupling corrosion. In fact, the passivating film, in this case, just partially impedes the entry of Cl^- ions, resulting in the formation of a layer of zinc chloride, $ZnCl_2$, detected by different characterization techniques, on sample surfaces [74] (Equation (15)):

$$Zn(OH)_{2\ (s)} + 2Cl^-_{(aq)} \rightarrow ZnCl_{2\ (s)} + 2OH^-_{(aq)} \tag{15}$$
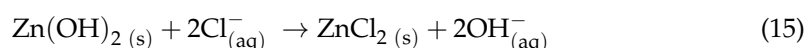
Thus, the $ZnO/Zn(OH)_2$ film is gradually weakened with the attack of aggressive ions leading to an increase in the kinetics of the corrosion process and, consequently, to an increase in the corrosion rate. Phosphates were detected for all conditions, but a clear crystallized $Zn_3(PO_4)_2$ layer was found just for PSS samples (Figures 2 and 6). It is worth noting that the formation of $Zn_3(PO_4)_2$ is of particular interest as it is reported to improve the cytocompatibility and antibacterial properties of Zn materials used for biomedical applications as well as to control the metal corrosion behaviour [37]. In fact, the precipitation of phosphate-rich salts, HPO_4^{2-}, PO_4^{3-}, have been reported to enhance passivation and reduce the corrosion rate [43]. For instance, in both HSS solutions, Zn and its alloys precipitate phosphates, depending on the local pH, temperature, HPO_4^{2-}/PO_4^{3-} concentration, presence of other anions/cations, solubility constant etc., forming a protective layer and hindering further corrosion [75]. Furthermore, since the Gibbs free energy (at 37 °C) for the formation of carbonates and phosphates is -197.82 kJ/mol and -198.55 kJ/mol, respectively [76], the slight difference of these two values implies that both compounds could precipitate in parallel according to Equations (10)–(14) to form Zn or Ca phosphates. This also does not hinder the formation of Ca phosphates.

Overall, the corrosion behavior of pure Zn appears to occur differently and depends on the type, composition and concentration of carbonates, phosphates and chloride ions in the three studied media and their atmospheric conditions.

5. Conclusions

Pure Zn degradation was evaluated by a 14-day static immersion test considering CO_2-poor and CO_2-rich- atmospheres and three solution media: Hanks' balanced salt (HSS), Dulbecco's phosphate-buffered saline (PSS) and physiological saline solution (NSS). Relevant differences in terms of degradation layer composition and morphology were found as well as different values of *CR*. The cross-correlated characterization carried out in this study allowed to observe that:

(a) ZnO or a mixed $ZnO/Zn(OH)_2$ degradation layer with $Zn_3(PO_4)_2 \cdot 4H_2O$ and $Zn(CO_3)_2$ precipitates were found on surfaces immersed in both HSS and PSS, independently of the atmosphere;

(b) A clear layer of crystallized $Zn_3(PO_4)_2 \cdot 4H_2O$ was detected just for the PSS condition;

(c) A $ZnO/ZnCl_2$ layer with amorphous carbonates precipitates was found on all surfaces immersed in NSS;

(d) Samples tested under a CO_2-rich atmosphere showed a more compact passivating layer, higher dimensions crystals and less cavities when tested in HSS, PSS and NSS, respectively, due to both buffering systems promoted by $CO_{2(g)}$ and the major protection contribution of carbonates;

(e) The highest *CR* was observed for pure Zn tested in NSS under ambient conditions due to the attack of aggressive Cl^- ions consuming the starting oxide/hydroxide degradation layer and the scarce protective contribution of the carbonates passivating layer.

Supplementary Materials: The following supporting information can be downloaded at: https://www.mdpi.com/article/10.3390/cryst13050753/s1, Figure S1: C1s HR details for samples under ambient condition; Figure S2: C1s HR details for samples immersed in 5 vol. % CO_2. Figure S3: O1s HR details for samples immersed in ambient atmosphere. Figure S4: O1s HR details for samples immersed in 5 vol. % CO_2.

Author Contributions: S.O.-M.: formal analysis, investigation, data curation, writing. S.G.: data curation, investigation, writing, reviewing and editing. A.L.R.-L.: methodology, investigation, formal analysis, data curation, supervision. C.P.: conceptualization, methodology, writing, supervision. D.M.: supervision, resources. All authors have read and agreed to the published version of the manuscript.

Data Availability Statement: Data is contained within the article or Supplementary Materials.

Conflicts of Interest: The authors declare no conflict of interest.

References

1.   Liu, Y.; Zheng, Y.; Chen, X.-H.; Yang, J.-A.; Pan, H.; Chen, D.; Wang, L.; Zhang, J.; Zhu, D.; Wu, S.; et al. Fundamental theory of biodegradable metals—Definition, criteria, and design. *Adv. Funct. Mater.* **2019**, *29*, 1805402. [CrossRef]
2.   Li, H.; Zheng, Y.; Qin, L. Progress of biodegradable metals. *Progr. Nat. Sci. Mater. Intern.* **2014**, *24*, 414–422. [CrossRef]
3.   Zheng, Y.; Gu, X.; Witte, F. Biodegradable metals. *Mater. Sci. Eng. R Rep.* **2014**, *77*, 1–34. [CrossRef]
4.   Schinhammer, M.; Hänzi, A.C.; Löffler, J.F.; Uggowitzer, P.J. Design strategy for biodegradable Fe-based alloys for medical applications. *Acta Biomater.* **2010**, *6*, 1705–1713. [CrossRef] [PubMed]
5.   Zhu, S.; Huang, N.; Xu, L.; Zhang, Y.; Liu, H.; Sun, H.; Leng, Y. Biocompatibility of pure iron: In vitro assessment of degradation kinetics and cytotoxicity on endothelial cells. *Mater. Sci. Eng. C* **2009**, *29*, 1589–1592. [CrossRef]
6.   Peuster, M. A novel approach to temporary stenting: Degradable cardiovascular stents produced from corrodible metal—results 6–18 months after implantation into New Zealand white rabbits. *Heart* **2001**, *86*, 563–569. [CrossRef]
7.   Zhang, E.; Chen, H.; Shen, F. Biocorrosion properties and blood and cell compatibility of pure iron as a biodegradable biomaterial. *J. Mater. Sci. Mater. Med.* **2010**, *21*, 2151–2163. [CrossRef]
8.   Hermawan, H.; Mantovani, D. Process of prototyping coronary stents from biodegradable Fe–Mn alloys. *Acta Biomater.* **2013**, *9*, 8585–8592. [CrossRef]
9.   Hermawan, H.; Purnama, A.; Dube, D.; Couet, J.; Mantovani, D. Fe–Mn alloys for metallic biodegradable stents: Degradation and cell viability studies. *Acta Biomater.* **2010**, *6*, 1852–1860. [CrossRef]

10. Fiocchi, J.; Biffi, C.A.; Gambaro, S.; Paternoster, C.; Mantovani, D.; Tuissi, A. Effect of laser welding on the mechanical and degradation behaviour of Fe-20Mn-0.6C bioabsorbable alloy. *J. Mater. Res. Technol.* **2020**, *9*, 13474–13482. [CrossRef]

11. Mouzou, E.; Paternoster, C.; Tolouei, R.; Chevallier, P.; Biffi, C.A.; Tuissi, A.; Mantovani, D. CO_2-rich atmosphere strongly affects the degradation of Fe-21Mn-1C for biodegradable metallic implants. *Mater. Lett.* **2016**, *181*, 362–366. [CrossRef]

12. Loffredo, S.; Gambaro, S.; Copes, F.; Paternoster, C.; Giguère, N.; Vedani, M.; Mantovani, D. Effect of silver in thermal treatments of Fe-Mn-C degradable metals: Implications for stent processing. *Bioact. Mater.* **2022**, *12*, 30–41. [CrossRef]

13. Sikora-Jasinska, M.; Chevallier, P.; Turgeon, S.; Paternoster, C.; Mostaed, E.; Vedani, M.; Mantovani, D. Understanding the effect of the reinforcement addition on corrosion behavior of Fe/Mg$_2$Si composites for biodegradable implant applications. *Mater. Chem. Phys.* **2019**, *223*, 771–778. [CrossRef]

14. Loffredo, S.; Gambaro, S.; de Andrade, L.M.; Paternoster, C.; Casati, R.; Giguère, N.; Vedani, M.; Mantovani, D. Six-month long in vitro degradation tests of biodegradable twinning-induced plasticity steels alloyed with Ag for stent applications. *ACS Biomater. Sci. Eng.* **2021**, *7*, 3669–3682. [CrossRef]

15. Wang, J.; Xu, J.; Hopkins, C.; Chow, D.H.; Qin, L. Biodegradable magnesium-based implants in orthopedics—A general review and perspectives. *Adv. Sci.* **2020**, *7*, 1902443. [CrossRef]

16. Chen, Y.; Xu, Z.; Smith, C.; Sankar, J. Recent advances on the development of magnesium alloys for biodegradable implants. *Acta Biomater.* **2014**, *10*, 4561–4573. [CrossRef] [PubMed]

17. Hartwig, A. Role of magnesium in genomic stability. *Mutat. Res./Fund. Mol. Mech. Mutagen.* **2001**, *475*, 113–121. [CrossRef]

18. Zhang, Y.; Xu, J.; Ruan, Y.C.; Yu, M.K.; O'Laughlin, M.; Wise, H.; Chen, D.; Tian, L.; Shi, D.; Wang, J.; et al. Implant-derived magnesium induces local neuronal production of CGRP to improve bone-fracture healing in rats. *Nat. Med.* **2016**, *22*, 1160–1169. [CrossRef]

19. Staiger, M.P.; Pietak, A.M.; Huadmai, J.; Dias, G. Magnesium and its alloys as orthopedic biomaterials: A review. *Biomaterials* **2006**, *27*, 1728–1734. [CrossRef]

20. Sandlöbes, S.; Pei, Z.; Friák, M.; Zhu, L.-F.; Wang, F.; Zaefferer, S.; Raabe, D.; Neugebauer, J. Ductility improvement of Mg alloys by solid solution: Ab initio modeling, synthesis and mechanical properties. *Acta Mater.* **2014**, *70*, 92–104. [CrossRef]

21. Zerankeshi, M.M.; Alizadeh, R.; Gerashi, E.; Asadollahi, M.; Langdon, T.G. Effects of heat treatment on the corrosion behavior and mechanical properties of biodegradable Mg alloys. *J. Magn. All.* **2022**, *10*, 1737–1785. [CrossRef]

22. Xie, J.; Zhang, J.; You, Z.; Liu, S.; Guan, K.; Wu, R.; Wang, J.; Feng, J. Towards developing Mg alloys with simultaneously improved strength and corrosion resistance via RE alloying. *J. Magn. All.* **2021**, *9*, 41–56. [CrossRef]

23. Tekumalla, S.; Seetharaman, S.; Almajid, A.; Gupta, M. Mechanical properties of magnesium-rare earth alloy systems: A review. *Metals* **2014**, *5*, 1–39. [CrossRef]

24. Virtanen, S. Biodegradable Mg and Mg alloys: Corrosion and biocompatibility. *Mater. Sci. Eng. B* **2011**, *176*, 1600–1608. [CrossRef]

25. Gambaro, S.; Nascimento, M.L.; Shekargoftar, M.; Ravanbakhsh, S.; Sales, V.; Paternoster, C.; Bartosch, M.; Witte, F.; Mantovani, D. Characterization of a magnesium fluoride conversion coating on Mg-2Y-1Mn-1Zn screws for biomedical applications. *Materials* **2022**, *15*, 8245. [CrossRef] [PubMed]

26. Kannan, M.B.; Raman, R.K.S. In vitro degradation and mechanical integrity of calcium-containing magnesium alloys in modified-simulated body fluid. *Biomaterials* **2008**, *29*, 2306–2314. [CrossRef]

27. Choudhary, L.; Raman, R.K.S. Magnesium alloys as body implants: Fracture mechanism under dynamic and static loadings in a physiological environment. *Acta Biomater.* **2012**, *8*, 916–923. [CrossRef] [PubMed]

28. Brady, M.P.; Rother, G.; Anovitz, L.M.; Littrell, K.C.; Unocic, K.A.; Elsentriecy, H.H.; Song, G.-L.; Thomson, J.K.; Gallego, N.C.; Davis, B. Film breakdown and nano-porous Mg(OH)$_2$ formation from corrosion of magnesium alloys in salt solutions. *J. Electrochem. Soc.* **2015**, *162*, C140–C149. [CrossRef]

29. Mostaed, E.; Sikora-Jasinska, M.; Drelich, J.W.; Vedani, M. Zinc-based alloys for degradable vascular stent applications. *Acta Biomater.* **2018**, *71*, 1–23. [CrossRef] [PubMed]

30. Mnatsakanyan, H.; Serra, R.S.I.; Rico, P.; Salmerón-Sánchez, M. Zinc uptake promotes myoblast differentiation via Zip7 transporter and activation of Akt signalling transduction pathway. *Sci. Rep.* **2018**, *8*, 13642. [CrossRef]

31. Kabir, H.; Munir, K.; Wen, C.; Li, Y. Recent research and progress of biodegradable zinc alloys and composites for biomedical applications: Biomechanical and biocorrosion perspectives. *Bioact. Mater.* **2021**, *6*, 836–879. [CrossRef]

32. Li, H.F.; Shi, Z.Z.; Wang, L.N. Opportunities and challenges of biodegradable Zn-based alloys. *J. Mater. Sci. Technol.* **2020**, *46*, 136–138. [CrossRef]

33. García-Mintegui, C.; Córdoba, L.C.; Buxadera-Palomero, J.; Marquina, A.; Jiménez-Piqué, E.; Ginebra, M.-P.; Cortina, J.L.; Pegueroles, M. Zn-Mg and Zn-Cu alloys for stenting applications: From nanoscale mechanical characterization to in vitro degradation and biocompatibility. *Bioact. Mater.* **2021**, *6*, 4430–4446. [CrossRef]

34. Wątroba, M.; Mech, K.; Bednarczyk, W.; Kawałko, J.; Marciszko-Wiąckowska, M.; Marzec, M.; Shepherd, D.E.T.; Bała, P. Long-term in vitro corrosion behavior of Zn-3Ag and Zn-3Ag-0.5Mg alloys considered for biodegradable implant applications. *Mater. Des.* **2022**, *213*, 110289. [CrossRef]

35. Hybasek, V.; Kubasek, J.; Capek, J.; Alferi, D.; Pinc, J.; Jiru, J.; Fojt, J. Influence of model environment complexity on corrosion mechanism of biodegradable zinc alloys. *Corros. Sci* **2021**, *187*, 109520. [CrossRef]

36. Vojtěch, D.; Kubásek, J.; Šerák, J.; Novák, P. Mechanical and corrosion properties of newly developed biodegradable Zn-based alloys for bone fixation. *Acta Biomater.* **2011**, *7*, 3515–3522. [CrossRef]

37. Su, Y.; Cockerill, I.; Wang, Y.; Qin, Y.-X.; Chang, L.; Zheng, Y.; Zhu, D. Zinc-based biomaterials for regeneration and therapy. *Trends Biotechnol.* **2019**, *37*, 428–441. [CrossRef]

38. Jain, D.; Pareek, S.; Agarwala, A.; Shrivastava, R.; Sassi, W.; Parida, S.K.; Behera, D. Effect of exposure time on corrosion behavior of zinc-alloy in simulated body fluid solution: Electrochemical and surface investigation. *J. Mater. Res. Technol.* **2021**, *10*, 738–751. [CrossRef]

39. Huang, S.; Wu, W.; Su, Y.; Qiao, L.; Yan, Y. Insight into the corrosion behaviour and degradation mechanism of pure zinc in simulated body fluid. *Corros. Sci.* **2021**, *178*, 109071. [CrossRef]

40. Liu, L.; Meng, Y.; Dong, C.; Yan, Y.; Volinsky, A.A.; Wang, L.-N. Initial formation of corrosion products on pure zinc in simulated body fluid. *J. Mater. Sci. Technol.* **2018**, *34*, 2271–2282. [CrossRef]

41. Zhou, Y.-L.; Li, Y.; Luo, D.-M.; Wen, C.; Hodgson, P. Microstructures, mechanical properties and in vitro corrosion behaviour of biodegradable Mg–Zr–Ca alloys. *J. Mater. Sci.* **2013**, *48*, 1632–1639. [CrossRef]

42. Lu, Y.; Bradshaw, A.R.; Chiu, Y.L.; Jones, I.P. Effects of secondary phase and grain size on the corrosion of biodegradable Mg–Zn–Ca alloys. *Mater. Sci. Eng. C* **2015**, *48*, 480–486. [CrossRef]

43. Shi, J.J.; Sun, W. Effects of phosphate on the chloride-induced corrosion behavior of reinforcing steel in mortars. *Cem. Concr. Compos.* **2014**, *45*, 166–175. [CrossRef]

44. Parfenov, E.V.; Kulyasova, O.B.; Mukaeva, V.R.; Mingo, B.; Farrakhov, R.G.; Cherneikina, Y.V.; Yerokhin, A.; Zheng, Y.F.; Valiev, R.Z. Influence of ultra-fine grain structure on corrosion behaviour of biodegradable Mg-1Ca alloy. *Corros. Sci.* **2020**, *163*, 108303. [CrossRef]

45. Wang, B.; Gao, W.; Pan, C.; Liu, D.; Sun, X. Effect of the combination of torsional and tensile stress on corrosion behaviors of biodegradable WE43 alloy in simulated body fluid. *J. Funct. Biomater.* **2023**, *14*, 71. [CrossRef]

46. Patel, S.; Miao, J.H.; Yetiskul, E.; Anokhin, A.; Majmundar, S.H. *Majmundar, Physiology, Carbon Dioxide Retention*; StatPearls Publishing: Treasure Island, FL, USA, 2022.

47. Hedberg, Y.S. Role of proteins in the degradation of relatively inert alloys in the human body. *Npj. Mater. Degrad.* **2018**, *2*, 26. [CrossRef]

48. Arthurs, G.; Sudhakar, M. Carbon dioxide transport. *Contin. Educ. Anaesth. Crit. Care Pain* **2005**, *5*, 207–210. [CrossRef]

49. Crystal, G.J. Carbon Dioxide and the Heart. *Anesth. Analg.* **2015**, *121*, 610–623. [CrossRef] [PubMed]

50. Gambaro, S.; Paternoster, C.; Occhionero, B.; Fiocchi, J.; Biffi, C.A.; Tuissi, A.; Mantovani, D. Mechanical and degradation behavior of three Fe-Mn-C alloys for potential biomedical applications. *Mater. Today Comm.* **2021**, *27*, 102250. [CrossRef]

51. *ASTM NACE/ASTMG31-21*; Standard Guide for Laboratory Immersion Corrosion Testing of Metals. ASTM International: West Conshohocken, PA, USA, 2012. Available online: http://www.astm.org (accessed on 1 January 2020).

52. Chen, Y.; Zhang, W.; Maitz, M.F.; Chen, M.; Zhang, H.; Mao, J.; Zhao, Y.; Huang, N.; Wan, G. Comparative corrosion behavior of Zn with Fe and Mg in the course of immersion degradation in phosphate buffered saline. *Corros. Sci.* **2016**, *111*, 541–555. [CrossRef]

53. Bowen, P.K.; Drelich, J.; Goldman, J. Zinc exhibits ideal physiological corrosion behavior for bioabsorbable stents. *Adv. Mater.* **2013**, *25*, 2577–2582. [CrossRef]

54. Zou, Y.; Chen, X.; Chen, B. Effects of Ca concentration on degradation behavior of Zn-x Ca alloys in Hank's solution. *Mater. Lett.* **2018**, *218*, 193–196. [CrossRef]

55. Mohan, A.C.; Renjanadevi, B. Preparation of zinc oxide nanoparticles and its characterization using scanning electron microscopy (SEM) and x-ray diffraction (XRD). *Proc. Technol.* **2016**, *24*, 761–766. [CrossRef]

56. Hosking, N.C.; Ström, M.A.; Shipway, P.H.; Rudd, C.D. Corrosion resistance of zinc–magnesium coated steel. *Corros. Sci.* **2007**, *49*, 3669–3695. [CrossRef]

57. Pawlig, O.; Trettin, R. Synthesis and characterization of α-hopeite, $Zn_3(PO_4)2 \cdot 4H_2O$. *Mater. Res. Bull.* **1999**, *34*, 1959–1966. [CrossRef]

58. Gordeeva, A.; Hsu, Y.-J.; Jenei, I.Z.; Carvalho, P.H.B.B.; Simak, S.I.; Andersson, O.; Häussermann, U. Layered zinc hydroxide dihydrate, $Zn_5(OH)_{10} \cdot 2H_2O$, from hydrothermal conversion of ε-$Zn(OH)_2$ at Gigapascal pressures and its transformation to nanocrystalline ZnO. *ACS Omega* **2020**, *5*, 17617–17627. [CrossRef] [PubMed]

59. Mouanga, M.; Berçot, P.; Rauch, J.Y. Comparison of corrosion behaviour of zinc in NaCl and in NaOH solutions. Part I: Corrosion layer characterization. *Corros. Sci.* **2010**, *52*, 3984–3992. [CrossRef]

60. Zeng, R.-C.; Li, X.-T.; Liu, L.-J.; Li, S.-Q.; Zhang, F. In vitro degradation of pure Mg for esophageal stent in artificial saliva. *J. Mater. Sci. Technol.* **2016**, *32*, 437–444. [CrossRef]

61. Törne, K.; Larsson, M.; Norlin, A.; Weissenrieder, J. Degradation of zinc in saline solutions, plasma, and whole blood. *J. Biomed. Mater. Res. B Appl. Biomater.* **2016**, *104*, 1141–1151. [CrossRef] [PubMed]

62. Eliaz, N. Corrosion of metallic biomaterials: A Review. *Materials* **2019**, *12*, 407. [CrossRef] [PubMed]

63. Asl, S.K.F.; Nemeth, S.; Tan, M.J. Hydrothermally deposited protective and bioactive coating for magnesium alloys for implant application. *Surf. Coat. Technol.* **2014**, *258*, 931–937. [CrossRef]

64. Bowen, P.K.; Shearier, E.R.; Zhao, S.; Guillory, R.J.; Zhao, F.; Goldman, J.; Drelich, J.W. Biodegradable metals for cardiovascular stents: From clinical concerns to recent Zn-alloys. *Adv. Healthc. Mater.* **2016**, *5*, 1121–1140. [CrossRef] [PubMed]

65. Liu, B.; Zheng, Y.F. Effects of alloying elements (Mn, Co, Al, W, Sn, B, C and S) on biodegradability and in vitro biocompatibility of pure iron. *Acta Biomater.* **2011**, *7*, 1407–1420. [CrossRef]

66. Zhu, Y.; Yu, X.; Pan, S.; Nong, P.; Kong, Q.; Wang, X.; Zhang, L.; Tan, S.; Zhu, Z. Dissolution of the smithsonite–rhodochrosite ($ZnCO_3$-$MnCO_3$) solid solutions in aqueous solution at 25 °C. *Chem. Geol.* **2022**, *602*, 120886. [CrossRef]

67. McMahon, M.E.; Santucci, R.J.; Scully, J.R. Advanced chemical stability diagrams to predict the formation of complex zinc compounds in a chloride environment. *RSC Adv.* **2019**, *9*, 19905–19916. [CrossRef] [PubMed]

68. Biesinger, M.C. Accessing the robustness of adventitious carbon for charge referencing (correction) purposes in XPS analysis: Insights from a multi-user facility data review. *Appl. Surf. Sci.* **2022**, *597*, 153681. [CrossRef]

69. Biesinger, M.C.; Lau, L.W.M.; Gerson, A.R.; Smart, R.S.C. Resolving surface chemical states in XPS analysis of first row transition metals, oxides and hydroxides: Sc, Ti, V, Cu and Zn. *Appl. Surf. Sci.* **2010**, *257*, 887–898. [CrossRef]

70. Duchoslav, J.; Arndt, M.; Keppert, T.; Luckeneder, G.; Stifter, D. XPS investigation on the surface chemistry of corrosion products on ZnMgAl-coated steel. *Anal. Bioanal. Chem.* **2013**, *405*, 7133–7144. [CrossRef] [PubMed]

71. Felker, D.L.; Sherwood, P.M.A. Zinc Phosphate ($Zn_3(PO_4)_2$) by XPS. *Surf. Sci. Spectra* **2002**, *9*, 106–113. [CrossRef]

72. Sander, R. Compilation of Henry's law constants (version 4.0) for water as solvent. *Atmos. Chem. Phys.* **2015**, *15*, 4399–4981. [CrossRef]

73. López, D.A.; Pérez, T.; Simison, S.N. The influence of microstructure and chemical composition of carbon and low alloy steels in CO_2 corrosion. A state-of-the-art appraisal. *Mater. Des.* **2003**, *24*, 561–575. [CrossRef]

74. Persson, D.; Thierry, D.; Karlsson, O. Corrosion and corrosion products of hot dipped galvanized steel during long term atmospheric exposure at different sites world-wide. *Corros. Sci.* **2017**, *126*, 152–165. [CrossRef]

75. Wang, B.; Li, Y.; Wang, S.; Jia, F.; Bian, A.; Wang, K.; Xie, L.; Yan, K.; Qiao, H.; Lin, H.; et al. Electrodeposited dopamine/strontium-doped hydroxyapatite composite coating on pure zinc for anti-corrosion, antimicrobial and osteogenesis. *Mater. Sci. Eng. C* **2021**, *129*, 112387. [CrossRef] [PubMed]

76. Zeng, R.; Lan, Z.; Kong, L.; Huang, Y.; Cui, H. Characterization of calcium-modified zinc phosphate conversion coatings and their influences on corrosion resistance of AZ31 alloy. *Surf. Coat. Technol.* **2011**, *205*, 3347–3355. [CrossRef]